Cover page

Leveraging Past Information and Machine Learning to Accelerate Land Disturbance Monitoring

Su Ye*[1], Zhe Zhu[1] and Ji Won Suh[1]

[1] Department of Natural Resources and the Environment, University of Connecticut, Storrs, CT, USA

This preprint has been submitted to *Remote Sensing of Environment* for peer review.

Twitter of the corresponding author: SuYe999

*Corresponding author: Su Ye (remotesensingsuy@gmail.com)

Leveraging Past Information and Machine Learning to Accelerate Land Disturbance Monitoring

Su Ye*[2], Zhe Zhu[1] and Ji Won Suh[1]

[1] Department of Natural Resources and the Environment, University of Connecticut, Storrs, CT, USA

Abstract

Near real time (NRT) monitoring of land disturbances holds great importance for delivering emergency aids, mitigating negative social and ecological impacts, and distributing resources for disaster recovery. Many past NRT techniques were built upon examining the overall change magnitude of a spectral anomaly with a pre-defined threshold, namely the unsupervised approach. However, their lack of fully considering spectral change direction, change date and pre-disturbance conditions often led to low detection sensitivity and high commission errors, especially when only a few satellite observations were available at the early disturbance stage, which could eventually result in a longer lag to produce a reliable disturbance map. For this study, we developed a novel supervised machine learning approach guided by historical disturbance datasets for accelerating land disturbance monitoring. This new approach first applied retrospective analysis based on historical Harmonized Landsat Sentinel-2 (HLS) datasets from 2015 to 2021 and several open disturbance products, in which various multifaceted change related predictors were extracted from satellite time series, followed by separate disturbance model construction for each consecutive anomaly number. Then, these models were applied for NRT prediction with a per-pixel disturbance probability with new observations (e.g., 2022 HLS images) ingested incrementally on a weekly basis. We developed this operational NRT system incorporating both unsupervised and supervised approaches. Latency and accuracy were evaluated against 3,000 samples randomly selected from five most influential disturbance events of United States in 2022 based on labels and disturbance dates interpreted from daily PlanetScope images. The evaluation showed that the supervised approach required 15 days (since the start of the disturbance event) to reach the plateau of its F_1 curve (where disturbances are detected with high confidence), seven days earlier with roughly 0.2 F_1 score improvement compared to the unsupervised approach (0.733 vs. 0.546 F_1 score). The further analysis showed the improvement was mainly due to the substantial decrease of commission errors (17.7% vs 44.4%). The latency component analysis indicated that the supervised approach only took an average of 4.1 days to yield the first disturbance alert at its fastest alerting speed when the NRT platform made a daily update. This finding highlighted the importance of past knowledge and machine learning for accelerating a NRT monitoring task.

Key words: Disturbance, Near real-time, Land Change, Time-series, Latency

*Corresponding author: Su Ye (remotesensingsuy@gmail.com)

1. Introduction

1.1 Near real-time monitoring

Land disturbance, often defined as any discrete event that occurs outside the natural variability of the land (Zhu et al., 2020), could fundamentally alter land surface composition, condition, and cover types, consequently disrupting ecosystem functioning such as biodiversity (Martínez-Ramos et al., 2016), productivity (Peters et al., 2013), carbon storage (Liang et al., 2014; Seidl et al., 2014). Land disturbances include natural hazards such as wildfire, flooding, and tornado, and a variety of land-use shifts led by anthropogenic activities. There is a pressing need for mapping land disturbance events in a timely manner, which will hold relevance for mitigating their social and ecological impacts (Verbesselt et al., 2012) and delivering emergency aids to protect lives and infrastructure (Field et al., 2012).

A large-scale Near-Real-Time (NRT) monitoring of land disturbances has been long limited by a lack of timely satellite data acquisition, until multiple global datasets became publicly available with reduced data latency and improved delivery service (Woodcock et al., 2008; Wulder et al., 2018). Earlier satellite-based NRT work were mainly based on coarse-resolution optical images such as the MODIS products, such as Terra-I system (Reymondin et al., 2012), DETER project (Shimabukuro et al., 2006) and the BFAST-monitor tool (Verbesselt et al., 2012), and later extended to the medium-resolution dataset owning to the free access policy of Landsat datasets, such as the Global Land Analysis and Discovery (GLAD) alerting system (Hansen et al., 2016), the Geobosques platform (Vargas et al., 2019) and Continuous Change Detection and Classification (CCDC)-adapted approaches (Pasquarella et al., 2017; Ye et al., 2021b). The recent NRT studies incorporates the Synthetic Aperture Radar (SAR) dataset (Bullock et al., 2022; Doblas et al., 2022; Eckerstorfer et al., 2019; Martinis et al., 2018) and 3-m daily PlanetScope data

(Francini et al., 2020), further reducing the observation lag by allowing for more frequent acquisition of satellite observations. On the other hand, some advanced approaches combined multiple sensors to shorten the time interval for collecting temporal observations (Reiche et al., 2018; Shang et al., 2022). For example, Shang et al. (2022) used the Harmonized Landsat Sentinel-2 (HLS) dataset which combines four satellite sensors (Landsat 8, Landsat 9, Sentinel-2A and Sentinel-2B) and successfully reduced the confirmation latency of a land disturbance to 35 days.

Despite various input dataset types, NRT disturbance algorithms are generally categorized into two broad groups: the cover-based and the anomaly-based approaches. The cover-based approach was built on the land cover classification and cover category change (or called land cover conversion) (Andela et al., 2022; Diniz et al., 2015; Francini et al., 2020; Giglio et al., 2009; Hansen et al., 2016; Reiche et al., 2021, 2018; Vargas et al., 2019). This approach, typically the Global Land Analysis & Discovery (GLAD) Alert system (Hansen et al., 2016), constructs a land-cover classification model based on historical or empirically selected samples, then apply the model to classify each newly collected image and detect new disturbance pixels if these pixels have been consistently classified as altered land cover categories. The recent emerging studies for NRT land cover mapping (Brown et al., 2022; Yu et al., 2022) could be potentially leveraged for the cover-based land disturbance monitoring as well. The cover-based approach often requires an additional step for reducing data noise and normalizing input images (Reiche et al., 2021, 2018) or simply assumes no seasonality for their targeted cover (Hansen et al., 2016). If a disturbance only induces within-type surface change (sometimes named as cover condition change), such as insect disturbance and drought, the cover-based approach might fail to alert the disturbance. Some advanced cover-based methods generated soft classification outputs as proxy, such as cover probability (Reiche et al., 2021, 2018) or cover fraction (Vargas et al., 2019), with a goal of addressing subtle change as a ‘continuous’ variable (e.g., forest loss). Nevertheless, these methods were only applicable to two-category classification scheme (e.g., forest vs. non forest) due to the complexity of multiclass probability combination.

The anomaly-based approach detects early disturbance signals by discriminating recent spectral anomalies against the baselines derived from satellite-based time series (Olsson et al., 2016; Pasquarella et al., 2017; Shang et al., 2022; Tang et al., 2019; Verbesselt et al., 2012; Ye et al., 2021a). The anomaly-based approach often operates in an unsupervised manner without needs of tackling land cover information. This approach first builds a baseline model by fitting historical time-series dataset from a stable period, and then continuously examine if the newly collected satellite observation has a spectral difference over a predefined threshold compared to its predicted reflectance, i.e., spectral anomaly. The new disturbance pixel will be confirmed if the minimum number of consecutive anomalies (namely “peek window”) is satisfied. The anomaly-based approach could exclude the noises such as data seasonality and other natural variation by incorporating cyclic trends and long-term trends into the baseline model. Also, benefited from directly detecting change magnitudes, the anomaly-based approach is capable of detecting subtle disturbances that does not directly alter land cover types using an adjusted change-magnitude threshold (Yang et al., 2022; Ye et al., 2021b).

Most cover-based or anomaly-based techniques require collecting a minimum number of consecutive observations ($conse$) for disturbance confirmation (e.g., $conse = 6$ in most CCDC-like approaches), as the temporal stability of a disturbance signal aids its differentiation from noisy signals. The setting of $conse$ is practically controlled by the user through algorithm configuration (Bullock et al., 2022). Arguably, it is common to employ less-than-required satellite observations for early disturbance alerting (Shang et al., 2022; Ye et al., 2021a), yet fewer post-disturbance observations for decision making comes at the cost of substantially increased commission errors. For example, Bullock et al. (2022) showcased over 80% commission errors in the initial 50 days since the disturbance occurrence date based on the sample-based agreement; likewise, Shang et al. (2022) reported over 80% commission errors when only one or two anomaly observations were identified. This was because these techniques discriminated disturbance signals only relying on their relatively higher overall spectral change magnitudes. When the post-disturbance data collection is short, the anomalies are more likely attributed to ephemeral and noisy signals (e.g., phenological variation, short-term weather extremes and even data noise), thereby compromising the detection accuracy. Consequently, a long collection of post-disturbance observations is still a must for most operational management tasks, if a NRT disturbance map with an acceptable commission rate is expected.

This study aims to develop a new supervised anomaly-based approach to greatly reduce detection latency and at the same time enhance the detection accuracy. The new approach was inspired by Retrospective Chart Review (RCR), a popular type of medical research design in which pre-recorded, patient-centered dataset are used to examine and study clinical characteristics (Gill and Kaplan, 2021; Kaji et al., 2014; Vassar and Matthew, 2013). One notable advantage of RCR is that it is easier to access conditions where there is a long latency from the initial exposure and the patient's diagnosis (Hess, 2004), so that the early symptoms could be identified. The valuable information gathered from RCR could be further applied to guide subsequent prospective studies. Similarly, the recent availability of numerous land cover datasets and disturbance products (Chuvieco et al., 2019; Johnson and Wittwer, 2008; Latifovic et al., 2016; Rollins, 2009) have provide an improved opportunity to achieve a timelier and more accurate NRT monitoring, combined with historical satellite datasets for extracting their temporal and spectral features.

Particularly, we are allowed to design methods to effectively extract early disturbance signals from historical time series, which can be further leveraged to construct machine learning models using this well-recorded disturbance event information. With enhanced model specificity and better capability to differentiate noise guided by labeled information, it is expected that retrospective disturbance analysis will improve both timeliness and accuracy, compared to the current anomaly-based approaches dominated by empirical thresholding. To our knowledge, historical dataset and analysis have been not systematically explored yet for the NRT disturbance mapping tasks. It is still unclear what disturbance predictors are extracted from satellite time series and how disturbance models are constructed for monitoring a variety of land disturbances at their different lag stages.

1.2 Lag components

To an operational NRT task, the latency is an intricacy impacted by five lag components, i.e., observation, data, sensitivity, confirmation, and production lag, from input, algorithm, and production perspectives (Fig. 1). Knowing the different proportions of individual latency source can better understanding timeliness potential and figuring out effective treatments. Note that compared to Fig.1 of Bullock et al. (2022), the assessments of sensitivity and production lags are newly proposed for this study.

The input latency is mainly affected by observation and data lags. Observation lag refers to the time interval between the disturbance occurrences and when the sensor collects the first clear observation, which could be related to a satellite revisiting cycle and weather condition; data lag is the delay between the first clear observation collection and this observation being preprocessed to a standard product ready for analytics, which is often systematic and shorter than one week (Bullock et al., 2022).

Algorithmic latency includes sensitivity and confirmation lags. Sensitivity lag refers to the day interval between the date for the first available data product and the date for an algorithm first alerting this disturbance. Sensitivity lag occurs where the disturbance signals is spectrally unobvious at the first observations (e.g., insect disturbances, selective logging), ranging from zero day (i.e., the quickest alert) for those dramatic disturbances, to infinity when the algorithm or the sensor is incapability of detecting the signal. Confirmation lag, also named as 'algorithm latency' in Bullock et al. (2022), is a lag between the first alert and the disturbance confirmation.

Lastly, production lag is the operational delay caused by the process of map production and delivery, closely linked to the updating frequency, and not well discussed yet in the past studies. For each processing, an NRT platform will ingest the new images released, map latest disturbance, and publish the NRT product. These steps are computationally expensive and time costly. Particularly for a large area monitoring system, it is often practically unfeasible to make a daily update, resulting in production lag due to the updating day interval.

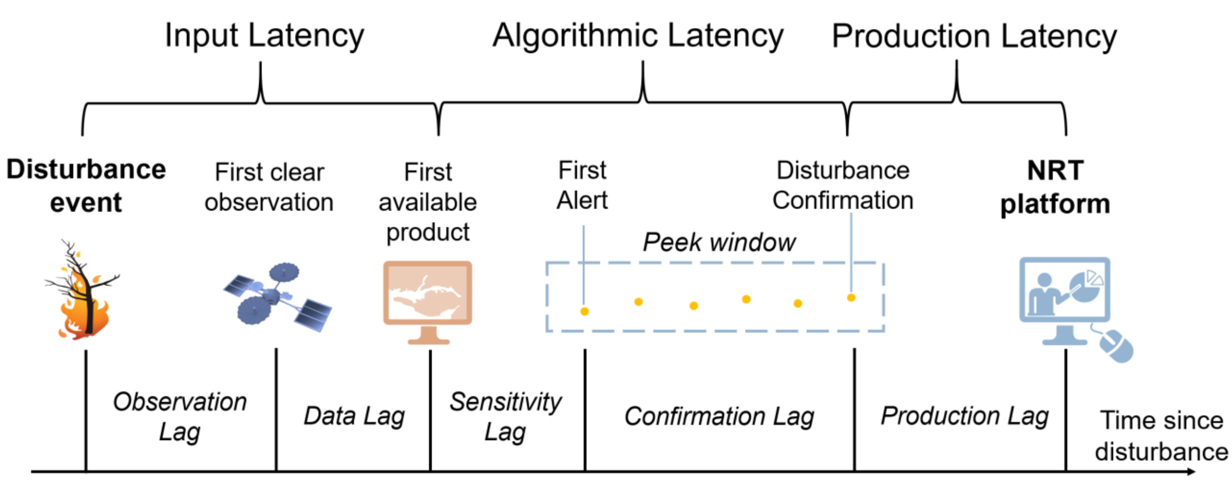

Fig. 1 Graphic explanations for the actual latency from an operational NRT disturbance task which is controlled by five lag components, i.e., observation, data, sensitivity, confirmation, and production lags.

The remainder of the paper will be organized as follow: we first introduce the study area and dataset used for this research (Section 2), then describe the design of an operational NRT system (Section 3); we will thoroughly compare latency and accuracy of the system adopting supervised against the unsupervised anomaly-based approach (Section 4.1), report their individual lag component assessment (Section 4.2), and exhibit distinction of latency curves and evaluation results from different disturbance events (Section 4.3); finally, we will discuss the comparative performance against other existing NRT methods as well as the disturbance confirmation dilemma (Section 5).

2. Study area and dataset

2.1 Study area

We chose five most influential disturbance events across the Conterminous United States (CONUS) in 2022, including three natural disasters, one forest disease and one human-induced land surface modification (Fig. 2).

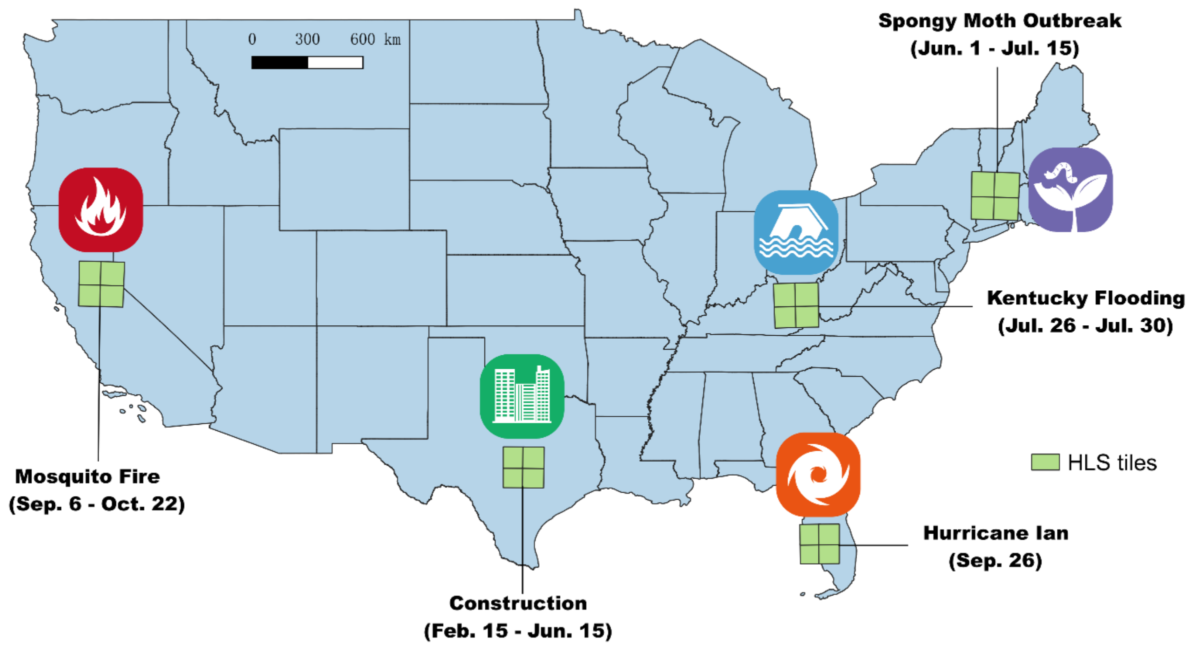

Fig. 2 Five selected sites for NRT monitoring of land disturbance events for 2022 in this study. For each event, four adjacent HLS tiles were used for the test.

Mosquito fire:

Mosquito fire was the largest wildfire of California in 2022. The massive fire began on September 6th and was 90% contained on October 4th, burning a total area of 31,075 hectares, mostly on forested regions of El Dorado and Placer counties; most of the fire regions (58%) experienced low soil burning severity (Teater, 2023). More than 11,117 people were evacuated, and 5,848 houses were threatened or damaged (Teater, 2023).

Spongy moth:

Spongy moth, formerly known as gypsy moth, has been a major forest disturbance type in New England. Sponge moth caterpillars hatch from egg mass in early May, begin feeding on the leaves of hardwood trees since early June, and reach peak defoliation by late June or early July as the larvae mature (Pasquarella et al., 2017). Sponge moth defoliation is an ephemeral and cyclic disturbance which occurs repeatedly every year in New England: trees often re-foliate from spongy moth attack at the summer, while moth-induced repeated defoliation combined with other stressors may lead to a long-term decline in forest health.

Hurricane Ian:

Hurricane Ian, which happened in September of 2022, was the deadliest hurricane to strike Florida since 1935. It peaked as a Category 5 hurricane with 260 km/h winds on September 28 when attacking the west coast of Florida (Karimiziarani and Moradkhani, 2023), causing major inland flooding and landfall in the counties such as Lee and Charlotte. The hurricane killed 149 people across Florida and produced catastrophic damage with loss around 113 billion at estimate (NOAA National Centers, 2023), including extensive tree and building damage due to strong wind and floods.

Kentucky flooding:

Between July 26 and July 30, 2022, due to sustained record-breaking rainfall, several devastating floods hit 15 counties in East Kentucky, such as Hidman, Perry and Prestonsburg counties. The deadly floods claimed the lives of 45 people and displaced thousands more. Entire homes and some communities were swept away by flood water, causing extensive damage to thousands of buildings, vehicles and other infrastructures in the region, with an estimated cost of over 1.5 billion dollars (NOAA National Centers, 2023).

Construction:

Texas has been one of the hotspots for construction projects in the past decade. Due to the lower cost of living and taxes, Texas, particularly Austin and Houston, has become a big draw to businesses and companies relocating from California and elsewhere. For example, Samsung started construction on a semiconductor manufacturing campus in the suburbs of Austin in 2022. Austin City ranked No.1 in the United States for the housing demand in 2022 with numerous construction sites for real estate developments (Baird, 2022), thereby was selected as the testing site for this study.

Table 1. Location, disturbance periods, and selected HLS tiles for the disturbance events to be tested for this study.

Disturbance Event	Impacted Region	HLS Tile IDs	Disturbance Period
Mosquito fire	Central California	10SFH, 10SFJ, 10SGH, 10SGJ	Sep. 6 – Oct. 22
Spongy moth	New England	18TXM, 18TXN, 18TYM, 18TYN	Jun. 1 – Jul. 15
Hurricane Ian	Southwest Florida	17RLK, 17RLL, 17RMK, 17RML	Sep. 26 – Sep. 28
Kentucky flood	Eastern Kentucky	17SKB, 17SKC, 17SLB, 17SLC	Jul. 26 – Jul. 30
Construction	Texas	14RNU, 14RNV, 14RPU, 14RPV	Feb. 15 – May 31

2.2 Datasets

Harmonized Landsat Sentinel-2 (HLS) dataset combines four satellite sensors (Landsat 8, Landsat 9, Sentinel-2A and Sentinel-2B satellites), providing the highest temporal resolution as 2-3 days (Claverie et al., 2018) among all medium-resolution (10-30 m) satellite datasets. Notably, for the latest version of HLS dataset (version 2.0), the Land Processes Distributed Active Archive Center approximately takes only two days of data lag to release the surface reflectance products based on our users' experience, with greatly reduced data lag. Therefore, the HLS datasets were selected as the time series inputs for this study. Each HLS tile has 3,660 rows and 3,660 columns with 30 m of pixel spacing in both directions, provided over projected map coordinates aligned with the Military Grid Reference System (MGRS). For each disturbance event, we chose four adjacent HLS tiles (2 by 2) for the NRT monitoring and the accuracy assessments (Fig. 1), and a total of 20 tiles and their 3 by 3 neighbor tiles were used for the study. For each tile, we downloaded all harmonized surface reflectance products from 2015 to 2021 for the retrospective analysis; during the later NRT monitoring stage, we downloaded the HLS images of 2022 in an increment of one week which is the predefined production interval for our test.

Besides, we collected four open-access annual CONUS disturbance products from 2016 – 2020, which will be used for labeling historical anomalies. They are 1) land cover transition map generated by differencing Land Change Monitoring, Assessment, and Projection (LCMAP) Primary Land Cover maps (Xian et al., 2022) between two neighbor years; 2) LANDFIRE Disturbance Products (Ryan and Opperman, 2013); 3) Landsat Collection 1 Level-3 Burned Area Science Product (Hawbaker et al., 2020); and 4) Aerial Detection Survey (ADS) insect activity dataset (Johnson and Wittwer, 2008).

We generated validation pixels by applying a stratified sampling approach on the accumulated NRT land disturbance maps. The accumulated NRT maps were made from merging all NRT detection maps from the assessment window for each disturbance; the assessment window is defined as the disturbance period with an extension of 15 days after a disturbance ends to take account of most delayed detections. We randomly sampled 300 pixels from the 'disturbance' and ‘no disturbance’ regions, respectively, in each accumulated NRT map (600 samples for an event), forming 3,000 samples in total for five disturbance events. For the response design, three experienced remote sensing experts interpreted the reference disturbance date for each sample pixel as the first date for their identifying visible disturbance signals from the Planet Explorer (https://www.planet.com/explorer/). The Planet Explorer provides free access to 3-m daily Planet images. Therefore we are capable of determining the actual disturbance date for reference sample pixel, which is more accurate than interpreting the first anomaly date from the time series (Shang et al., 2022; Ye et al., 2023, 2021a) or using the date right in-between the first anomaly date and the last pre-disturbance observation date (Bullock et al., 2022; Reiche et al., 2018). While the occasional cloud/shadow contamination or missing dataset in PlanetScope still might cause inaccurate interpretation of the exact disturbance date, we think such impacts are negligible because 1) Planetscope images have provided the densest optical images as daily observations; 2) the beginning dates for some disturbance events for our experiments (such as Hurrican Ian and Mosquito Fire) have been well recorded and ascertained to be directly adopted. The labeling process with used PlanetScope images was showcased in Section S1 of the supplementary material.

3. Methodology

A two-stage workflow was designed for this new approach (Fig.3). For the first stage of “retrospective disturbance analysis”, we extracted relevant disturbance predictors and built a series of disturbance models from historical disturbance and image dataset; for the second stage of “Near Real-time Monitoring”, we applied a NRT disturbance mapping based on the disturbance models incrementally with a step of one week for the year of 2022.

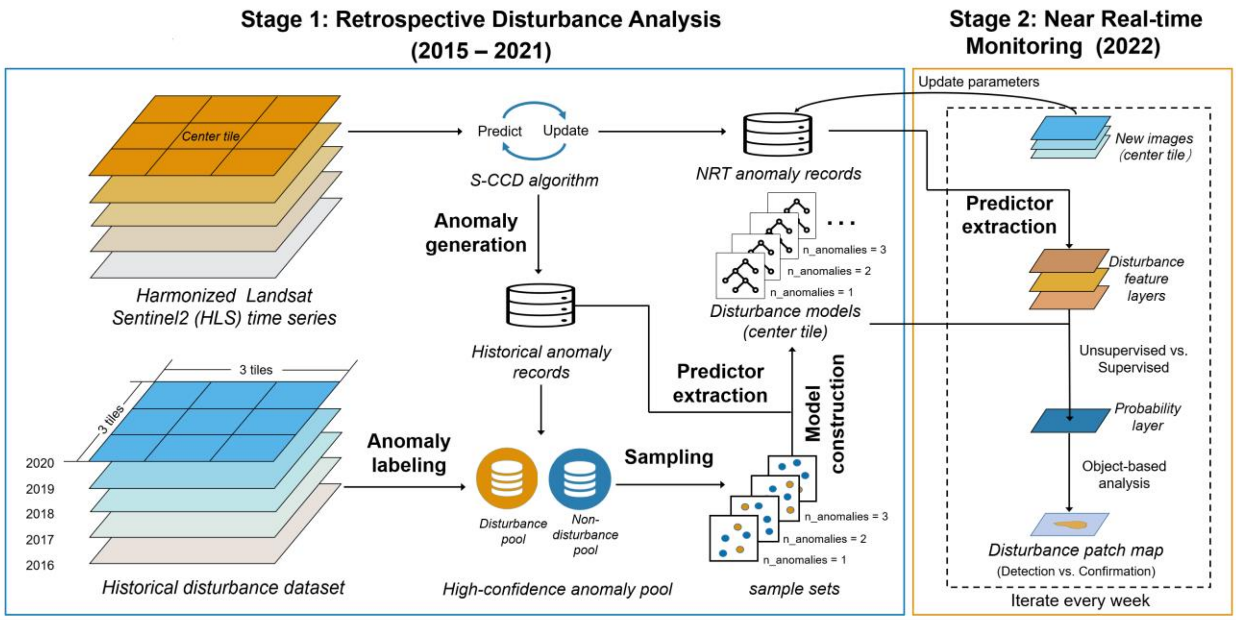

Fig. 3. A two-stage workflow of the supervised near real-time monitoring approach proposed for this study.

3.1 Stage 1: Retrospective Disturbance Analysis

3.1.1 Anomaly generation

We leveraged historical HLS dataset (2015-2021) to simulate local spectral anomalies for the NRT condition at a per-tile basis. For each HLS tile to be monitored, Stochastic Continuous Change Detection (S-CCD) (Ye et al., 2021a), a near real-time adaptation of Continuous Change Detection and Classification (CCDC) (Zhu and Woodcock, 2014), was applied to detect historical spectral anomalies. S-CCD incorporates the Kalman filter into the CCDC algorithm and recursively updates the anomaly records (see Table S1 in the supplementary), instead of reconstructing the model from the scratch for each new observation (Ye et al., 2021a). The short-memory nature in S-CCD saves disk space from removing the historical images and speeds up the computation by skipping the step of refitting the time-series model, thereby improving model efficiency for large area NRT monitoring. An improvement we made on Ye et al. (2021a) is to let

S-CCD produce two types of breakpoints in one run for historical dataset, 1) spectral anomalies and 2) structural breakpoints. Spectral anomalies are a group of breakpoints triggered by an aggressive parameter setting with a goal of yielding both disturbance and other non-disturbance anomalies (e.g., phenology shifts and ecosystem recovery). To produce spectral anomalies, we applied a shorter *conse* as three consecutive observations against the default six minimum consecutive anomaly number, and a lower change threshold of 0.90 (the default *chg_t* is 0.99), ensuring most subtle disturbance pixels to be inclusive in the spectral anomaly pool (Cohen et al., 2017). Different with the normal CCDC's way for handling breakpoints, S-CCD algorithm will skip the model initialization for spectral anomalies but only save the current anomaly records (see Table S1), considering that the Kalman filter can self-adjust model coefficients with such-like local fluctuations (Ye et al., 2021a). Structural breakpoints refer to a group of breakpoints that lead to significant structural change of the time series, where it is essential to refit a new harmonic curve by using new observations of at least one year to guarantee the model predictability (Zhu et al., 2020). We adopted a more conservative parameter set to generate structural breakpoints, *chg_t* = 0.9999, *conse* = 8, for identifying structural breakpoints. When the last observation of a historical time series was processed, the anomaly records, which represented the current spectral status, were saved out into the disk for the second stage.

3.1.2 Anomaly labeling

We combined two sources of disturbance maps, respectively from anomaly generation and historical disturbance products, to develop high-confidence spectral anomaly pools. An anomaly-based disturbance map was produced from anomaly records by applying the disturbance-extraction strategy proposed in section 3.3.6 in Zhu et al. (2020). On the other hand, we generated an annual product-based disturbance potential map (2016-2020) by fusing four previously mentioned open disturbance products, and the pixels were labeled as ‘disturbance’ if this pixel falls within the disturbance region in at least one open disturbance product. We extracted the high-confidence disturbance pixels from the overlapped disturbance regions between anomaly-based and product-based maps into a disturbance anomaly pool. Those pixels labeled as “disturbance” only in anomaly-based maps are spectral anomalies uncovered by historical disturbance regions and hence represent noisy signals, so we sort them into a non-disturbance anomaly pool.

For each HLS tile, we generated spectral anomalies at an annual basis, and then combined training data from a 3 by 3 HLS tile window centered at the targeted tile, with a temporal length of the recent five years (2016 - 2020) into one disturbance and another non-disturbance anomaly pool, where the center tile is the tile to be monitored. There are two primary motivations for the 3 by 3 spatiotemporal tile window design: 1) the machine learning model could be developed with a better capability of dealing with disturbance variability using sample acquisition from a larger spatial extent and a longer disturbance history; 2) 3 by 3 tile window significantly decreases the variation of local models between two neighborhood tiles, avoiding artifacts on the boundaries of the two tiles (Brown et al., 2019).

3.1.3 Predictor extraction

We extracted 15 disturbance-related predictors (Table 2) from each historical anomaly record, which could be categorized into the pre-disturbance and post-disturbance groups. Fig. 4 illustrates these disturbance-related predictors using a sample time series. Five HLS spectral bands, i.e., green, red, NIR, SWIR1 and SWIR2 bands, were considered. We remained the three predictors used in the COntinuous monitoring of Land Disturbance (COLD) algorithm (Zhu et al., 2020) for the disturbance-related breakpoint decision, i.e., 1) normalized change intensity (Eq. 8 in Zhu et al., 2020), 2) spectral consistency angle (Eq. 9 in Zhu et al., 2020), and 3) multispectral change magnitudes (see Eq. 10 in Zhu et al., 2020) to include spectral change angle information. Besides, we also included 4) change date to incorporate seasonality, 5) span of anomaly days for data temporal density, and 6) multispectral pre-change reflectance to depict land cover spectral condition prior to spectral anomalies being detected.

Table 2. definition of 15 disturbance predictors used for the NRT disturbance prediction

Predictor name	Description	Number	Category
1. Normalized change magnitude	$CM_{normalized} = \sum_{i=1}^{5}(\frac{CM_i}{RMSE_i})^2$	1	
2. Multispectral change Magnitudes	$CM_i = \rho_{i,dist\_dat} - \hat{\rho}_{i,dist\_dat}, i = 1,2,3,4,5$	5	
3. Spectral consistency angle	$angle = \frac{1}{n-1}\sum_{j=1}^{n-1}\beta_{j,j+1}$	1	Post-disturbance
4. Disturbance date	$sin_{doy} = sin\left(\frac{2\pi}{T}doy_{dist\_dat}\right)$, $cos_{\mathrm{doy}} = \sin\left(\frac{2\pi}{T}doy_{dist\_dat}\right)$	2	
5. Anomaly span	$ndays = lastobs\_dat - dist\_dat$	1	
6. Multispectral pre-disturbance reflectance	$\hat{\rho}_{i,dist\_dat} = a_{0,i} + \sum_{k=1}^{3}\left(a_{k,i}\cos\left(\frac{2\pi}{T}x\right) + b_{k,i}\sin\left(\frac{2\pi}{T}x\right)\right) + c_{1,i}x,\ \mathrm{i} = 1,2,3,4,5$	5	Pre-disturbance

Note: $\mathrm{CM_i}$ and $RMSE_i$ are the individual change magnitude and Root Mean Square Error of the ith band; $\rho_{i,dist\_dat}$ and $\hat{\rho}_{i,dist\_dat}$ are the actual and the predicted reflectance of the ith band; n is the current consecutive anomaly number; $\beta_{j,j+1}$ is the change-vector angle from jth to $j+1$th anomaly; $lastobs\_dat$ and $dist\_dat$ are the last available observation date and the disturbance starting date; doy is the date of year; $a_{0,i}$, $a_{k,i}$, $b_{k,i}$ and $c_{1,i}$ are the harmonic coefficients for the ith band; k is the temporal frequency of the harmonic components.

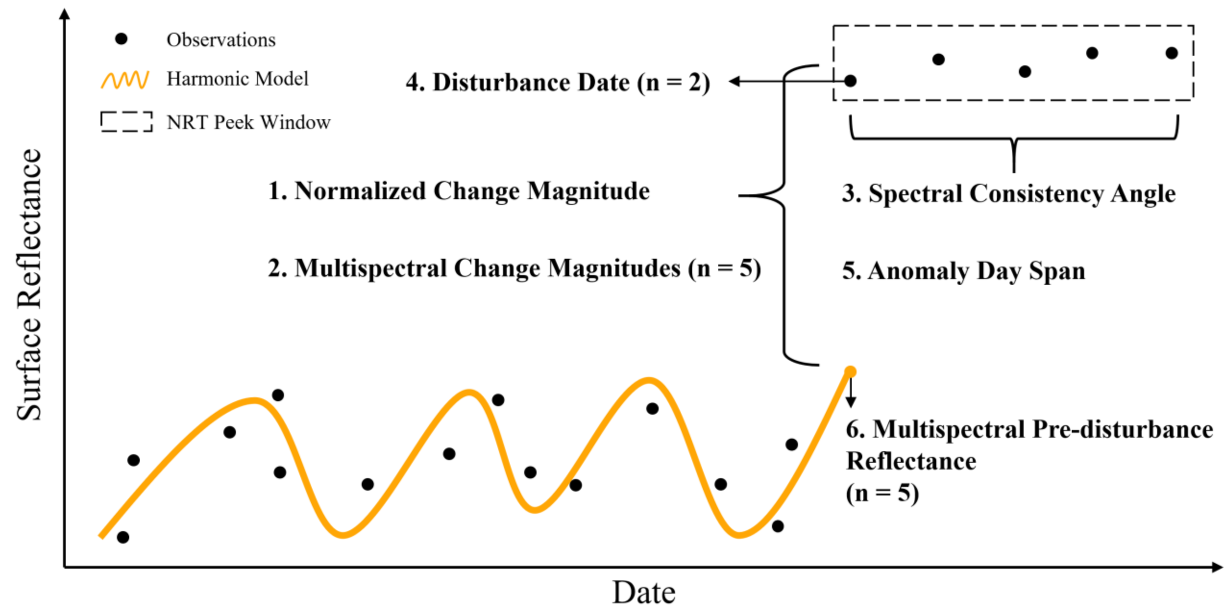

Fig. 4. Graphic illustration of the disturbance-related predictors used for this study ("n" means the variable number).

3.1.4 Model construction

To enhance the model specificity for different NRT stages, we individually established sample sets and disturbance models for different lengths of peek windows, i.e., the current number of consecutive anomalies ($n_{anomalies}$). A total number of 10,000 samples was empirically selected for each tile. Zhu et al. (2016) suggested a total of 20,000 samples for the Landsat-based classification and an HLS image (3,660 * 3,660) occupies only half of the total pixel number of the Landsat scene (5,000 * 5,000). To evenly distribute these 10,000 samples across the sample years, we allocated 2,000 samples for each tile in each year. A proportional sampling was used as it has shown superiority over a balanced sampling for a classification scheme (Brown et al., 2019; Zhu et al., 2016). Practically, there are far fewer disturbance anomalies compared to the non-disturbance anomalies, which requires applying the minimum categorical proportion to avoid the disturbance category to be under-represented. The trickier is the omission and commission rates both increased due to added noisy signals with less consecutive anomalies, but we preferred a low omission error rate over time, particular for the lag is short. As such, a function for the minimum proportion was designed based upon $n_{anomalies}$, so that the higher minimum proportion of disturbance categories could be assigned to the shorter $n_{anomalies}$ (i.e., the earlier disturbance stage) to keep a roughly temporally consistent omission error rate:

$$Prop_{disturb} = Prop_{base} + (CONSE - n_{anomalies}) * slope$$

Where $CONSE$ is a constant, the number of consecutive anomaly observations to detect a structural breakpoint ($CONSE = 8$), $Prop_{base}$ is the baseline proportion when the $n_{anomalies}$ reaches the maximum, and the parameter $slope$ controls decreasing impacts of $n_{anomalies}$ on $P_{disturb}$. When $n_{anomalies}$ was the minimum (i.e., $n_{anomalies} = 1$), $P_{disturb}$ reached the highest so that the category of disturbance anomalies was oversampled the most to keep up the omission error rate. The parameter sensitivity test (see Section S3 of the supplementary material) reveals $Prop_{base} = 0.1$ and $slope = 0.02$ is the only group that keeps an acceptable overall accuracy while maintaining a low omission rate across all $n_{anomalies}$.

For each $n_{anomalies}$ (i.e., 1, 2, 3, …, 8), we trained a random-forest model ($ntrees$ = 100) to make a binary classification (disturbance vs. no disturbances) using each individual sample set. Eight disturbance models were built for the NRT monitoring stage.

3.2 Stage 2: Near Real-time Monitoring

Starting from January 1st, 2022, we iterated a workflow of near real-time monitoring to process the newly collected images until the end of 2022. The workflow was operated incrementally at a step of one week, i.e., the system updating frequency was one week. The workflow ingested images collected, updated the NRT anomaly records and then extracted 15 disturbance-related predictors listed in Table 2 for each pixel. We tested and compared two ways for generating disturbance probability: (1) the proposed method based on the models trained from historical datasets (called supervised) and (2) the traditional anomaly method based on an empirical change-magnitude threshold (called unsupervised). For the supervised probability, we input the predictor vector associated with into the different disturbance models based on the current consecutive anomaly number at pixel-level (we used 0.9 chi-square probability for detecting anomalies, same as “anomaly generation” for Stage 1); then predicted its random-forest disturbance probability. For the unsupervised probability, we used the CCDC threshold for the normalized change magnitude used in the “Land Change Monitoring, Assessment, and Projection” project (Brown et al., 2019), the chi-square probability of 0.99, to detect anomalies, and then filtered the breakpoints attributing to the ‘greener’ trend based on (Eq. 10 of Zhu et al., 2020)):

$$\Delta\text{Red} < 0.02\ \&\ \Delta\text{NIR} > -0.02\ \&\ \Delta\text{SWIR1} < 0.02$$

where ΔRed, ΔNIR and ΔSWIR1 are the spectral change magnitudes of the RED, NIR and SWIR1 band for the breakpoint. The unsupervised probability was computed as the current consecutive anomaly number divided by the maximum anomaly number ($CONSE = 8$). For example, if there are six anomalies at the end of the current time series, the probability is 6 / 8 = 75%.

To generate spatially complete disturbance patches, the floodfill segmentation algorithm was first applied to the two disturbance probability layers (Ye et al., 2023). For the supervised probability layer, we remained the disturbance regions as the disturbance patches with an average disturbance probability > 50%; for the unsupervised-probability layer, we labeled the patches as their average probability >= 12.5%, so that the disturbance identification was possible even when one anomaly observation was captured, as consistently as the supervised-probability approach.

Finally, the identified disturbance patches were categorized into two levels of the NRT products based upon the current patch-level anomaly number. We assigned the disturbance patches with averagely less than six consecutive anomalies into "detection level", and otherwise "confirmation level". We used the confirmation threshold as six anomalies, considering most CCDC-like algorithms use six observations as the minimum required anomaly number (Brown et al., 2019; Ye et al., 2021a; Zhu et al., 2020). When one workflow was completed for a monitoring interval, we saved two levels of the disturbance products with their disturbance attributes into the database. The polygon-based attributes include the first anomaly date, the last anomaly date, the production date (we set it as the last day of each week). As our experiments were performed in early 2023, all HLS dataset for 2022 have been available for downloading and hence the data lag is zero. To keep close to the real latency for the operational monitoring, we manually set the data lag as two days of HLS data lag and added it to all production dates. It is worth mentioning that our comparative evaluation mainly focuses on the detection-level products, though both the detection- and confirmation-level results will be assessed and reported. This is because the detection level is practically more relevant for an NRT platform as it can enable the timelier monitoring (<10 days) and provide important base maps for high-resolution applications. We developed an operational platform to visualize the NRT results based on Google Earth Engine platform (https://gers.users.earthengine.app/view/nrt-conus).

3.3 Accuracy and latency assessment

We used the sigmoid framework proposed by Bullock et al. (2022) to comparatively assess the unsupervised and supervised approach. The sigmoid framework incorporates both omission and commission of disturbance alerts as a function of lag, which produces more comprehensive assessment than other NRT assessment metrics that only focused on the disturbance cases being correctly identified (Bullock et al., 2022), such as Mean Time Lag (MTL) (Reiche et al., 2018). In this study, the omission error at a certain lag is defined as the case when a disturbance sample is not hit by the disturbance patches from the recent NRT results; the commission error is defined as the case when a non-disturbance sample is included in one disturbance patch.

Following the sigmoid framework, we graphed omission, commission and F_1 score as sigmoid curves for incremental values of the total lag (i.e., production date minus disturbance date), allowing for a thorough comparison of detection effectiveness at a full range of latency. F_1 score is a harmonic mean of inverse omission and commission error rate:

$$F_1 = 2 * \frac{(1 - omission) * (1 - commission)}{(2 - omission - comission)}$$

Two lag metrics generated from the sigmoid curves were used as the primary tool to assess "lag-accuracy" performance, the Initial Delay and Level Off Point. The Initial Delay is assigned to the date that 2% of the total disturbance pixels are detected, representing the shortest time of an algorithm for beginning to alert a disturbance event. The Level Off Point, the time when F_1 score is just stabilized, is computed as the date that has the maximum y for a virtual curve from rotating 45 degrees around the line of connecting the beginning and end points of the sigmoid curve (Bullock et al., 2022). The x coordinate of Level Off Point indicates the shortest lag to reach the maximum F_1 score, and the y coordinate points to the maximum overall performance.

Moreover, we assessed the individual contribution of the five lag sources given in Fig. 1. We generated individual lags for each disturbance sample following the definitions given in Table 3, and then computed the mean statistics of each lag component. It is noteworthy that the sum of all the lag sources is equivalent to MTL, a lag metric commonly used in the previous studies (Shang et al., 2022; Ye et al., 2021a); the sum of all except the confirmation lag is named as Mean Time Lag for the First Alert (MTL_f) (Reiche et al., 2018), which is actually the average time between the reference disturbance date and the date for capturing the first anomaly. We will report MTL and MTL_f as well for comparison to other existing studies.

Table 3. Definition of five lag components for a reference sample

Lag components	Definition
Observation Lag	Day interval between the reference disturbance date and the first clear observation date
Data Lag	Constant value as two days
Sensitivity Lag	Day interval between the first clear observation date and the first anomaly date detected
Confirmation Lag	Day interval between the first and the last anomaly date detected for a peek window
Production Lag	Day interval between the last anomaly date and the date being officially confirmed by the platform

4. Results

4.1 Unsupervised vs. Supervised

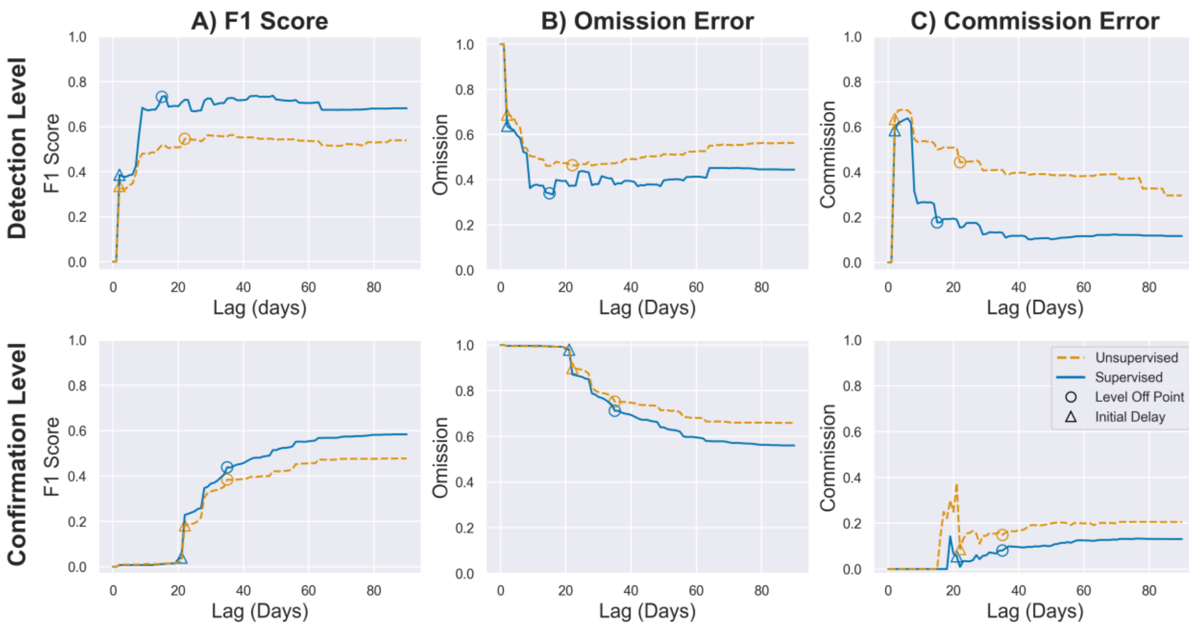

Fig. 5. Comparison of the unsupervised and supervised detection approaches on sigmoid curves at detection and confirmation levels based on a total of 3,000 evaluation samples from the five disturbance sites. Omission error, commission error and F_1 score are respectively plotted as a function of total lag (the sum of five lag components) within a tolerance window of 0 to 90 days. Two key latency metrics, Initial Delay and Level Off Points, are marked on the curves as "circle" and "triangle".

Fig. 5 shows the sigmoid curves for the unsupervised (the traditional anomaly-based) and the supervised (the proposed) NRT approach based upon all evaluation samples from the five testing sites (n = 3,000, 50% are disturbance samples). Table 2 listed their key lag metrics . Generally, F_1 score curves for the two approaches both began to increase around the Initial Delay (Fig. 5A); with the time going forward, F_1 was gradually rising because more post-disturbance observations became available both temporally and spatially, and eventually plateaued at the Level Off Point (Fig. 5A). The sigmoid curves of the two approaches were almost fully overlapped before their Initial Delay (2 days for the detection level, and ~21 days for the confirmation level), and became divergent afterward: F_1 sigmoid curve of the supervised approach ("blue") became consistently higher than that of the unsupervised approach ("yellow"). Particularly at the detection level, the supervised approach only took 15 days to reach the Level Off Point with 0.733 F_1 score, which had seven days quicker and almost 0.2 F_1 improvement than the unsupervised (the unsupervised: 22 days, 0.546 F_1 score, see Table 2).

Table 4. Comparison of the unsupervised and supervised approaches on lag, omission error, commission error and F_1 score at their Initial Delay and Level Off Point. The bold font highlights the lag/accuracy difference between the two approaches.

	Detection Level							
	Initial Delay				Level Off Point			
	Lags (Days)	Omission Error	Commission Error	F_1	Lags (Days)	Omission Error	Commission Error	F_1
Unsupervised	2	68.8%	63.5%	0.336	**22**	46.4%	**44.4%**	**0.546**
Supervised	2	63.9%	58.5%	0.386	**15**	34.0%	**17.7%**	**0.733**
	Confirmation Level							
	Initial Delay				Level Off Point			
	Lags (Days)	Omission Error	Commission Error	F_1	Lags (Days)	Omission Error	Commission Error	F_1
Unsupervised	22	89.9%	8.7%	0.182	35	75.2%	14.9%	0.384
Supervised	21	98.0%	0.6%	0.040	35	71.2%	8.1%	0.439

By investigating the error components, the supervised presented a consistently lower omission (Fig. 5B) and commission rates (Fig. 5C) than the unsupervised approach over time after the Initial Delay. Particularly, the supervised achieved much lower commission error rate than the unsupervised by approximately 27% at the detection level (17.7% vs. 44.4%, Table 4). This revealed the primary advantage of incorporating historical datasets was in alleviating overdetection. Fig. 6 showcased a sample pixel under the effects of climate variability that was misclassified as "disturbance" by the unsupervised approach. Its NIR time series experienced a significant increase at the breakpoint (Fig.6A), which was related to the earlier leaf-on date for the year of 2022 as no obvious disturbance signals were noticed from HLS image chips (Fig. 6B). The unsupervised approach captured the break as "disturbance" because the overall change magnitude was larger than the predefined threshold (the chi-square probability of 0.99), while the supervised correctly ignored it (Fig. 6C) through a comprehensive examination on change magntiudes, pre-change features, change season, change direction based on a machine learning technique.

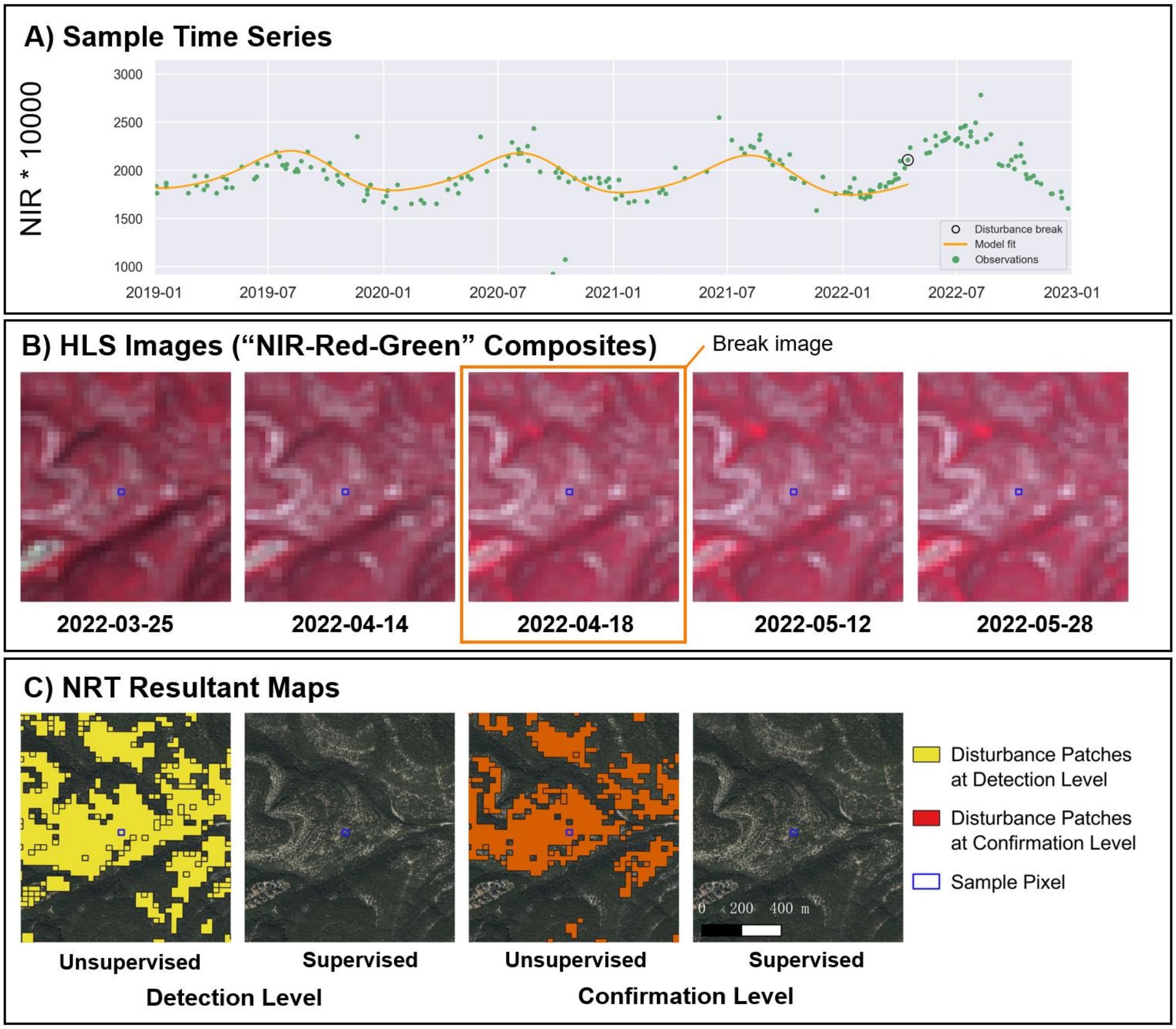

Fig. 6. An example site (-97.947, 30.339) for commission errors produced by the unsupervised approach. The HLS time series (A) shows a structural breakpoint induced by increasing NIR which was possibly related to phenological shifts, while no obvious disturbance signal was found from inspecting the HLS images (B). The supervised approach exhibited superiority for suppressing such over-detection by modeling disturbance and commission errors during the retrospective analysis stage (C).

Fig. 7 is an example to show that the supervised approach also could decrease omission errors. The sample pixel was experiencing spongy moth damage with a medium-level NDVI drop on June of 2022 (Fig. 7A and B). While no structural break was detected so that the model fitting kept continuous, the supervised approach still analyzed the spectral anomaly associated with each observation and predicts disturbance probability. Therefore, the supervised approach accurately delineated subtle change induced by spongy moth (Fig. 7C). However, the unsupervised approach missed most damage at the confirmation level (Fig. 7C) as it regorously detected the disturbance breaks based upon a threshold of 0.99 chi-square probability.

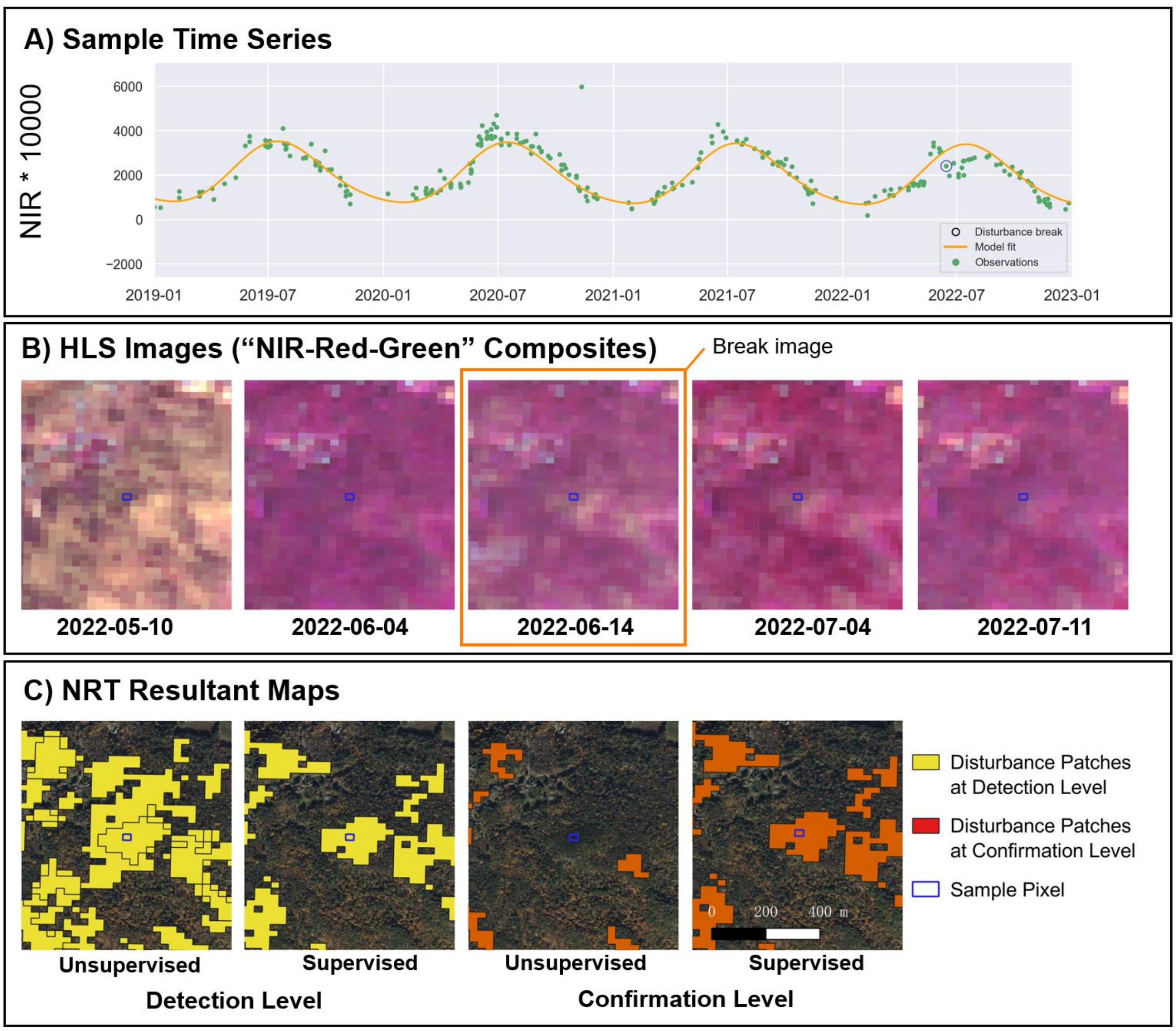

Fig. 7 An example site (-73.377, 41.946) for omission errors produced by the unsupervised approach. The HLS time series (A) shows a time series impacted by spongy moth damage, with the disturbance break detected by the supervised approach marked as "black circle" in (A). The damage has been verified by color change ("white spots") within HLS images (B).

The NRT results (C) present that the unsupervised approach totally missed the disturbance patches at the confirmation level.

Comparing the detection and confirmation level, the accuracies at the detection level were higher than at the confirmation level for both approaches. Particularly, the omission errors are significantly lower at the detection level (e.g., 0.340 vs. 0.712 at the Level Off Point for the supervised approach, Table 2). This finding was contrary to most past NRT studies, in which the confirmation results achieved the better overall accuracies owing to more consecutive anomalies involved for the decision. The higher performance for the detection level was possibly due to an inclusion of two ephemeral disturbances into the five study sites (344 / 830 disturbance cases), causing an unrealistically higher proportion for the ephemeral disturbance type, in which the detection level could better capture them because it involves consecutive observations. The unsupervised and supervised approaches presented the same lag days to reach their Level Off Points for the confirmation level (35 days) because the two approaches both applied $conse = 6$ hence similar confirmation lag. The delay relating to a collection of six consecutive observations dominated the total lag (~77% of the total lag, see Section 4.2). However, the supervised approach still achieved a relatively better F_1 score at the confirmation level (0.439 vs. 0.384 at Level Off Point). Another distinction between the detection and the confirmation level was that the confirmation level required much longer lag to reach Initial Delay (~21 days), reflecting the low bound of the lag days required to acquire six consecutive anomalies.

4.2 Lag Component Evaluation

Fig. 8 displays assessments on different lag components of the two approaches. The total lag of the two approaches, MTLs are close (39.4 vs. 38.8 days), which is mainly due to 1) the ambiguity in reporting independent temporal metrics with ignorance on spatial accuracy (i.e., omission and commission error rates) (Bullock et al., 2022) ; 2) the total lags of the two approaches were dominated by their similar confirmation lag (~77%) as their required anomaly number are both set as six. In comparison, the supervised approach yielded much lower sensitivity lags (0.1 vs 1.1 days), making its MTL_f shorter than the unsupervised by 10% (9.1 vs. 10.0 days). This revealed the advantage of the supervised approach for the early alerting of the disturbance especially when the signal was not pronounced. The observation lags were both averagely 2.0 days, which was mainly caused by HLS revisiting cycle and weather condition. The average production lags of the two approaches were both around 5.0 days, slightly higher than expected as a half of the updating interval (3.5 days). It is noteworthy that MTL and MTL_f of the two approaches did not present sufficient differences as their sigmoid curves showed (Fig. 5), which echoed the viewpoint that they are problematic for latency assessment as the two latency metrics were calculated based on their own correctly identified samples (unsupervised vs. supervised: 287 vs. 370 cases), ignoring their omission and commission errors (Bullock et al., 2022). A high rate of omission errors and commission errors caused incomplete patch detection and too many noisy signals, which will eventually lead to a mapping delay.

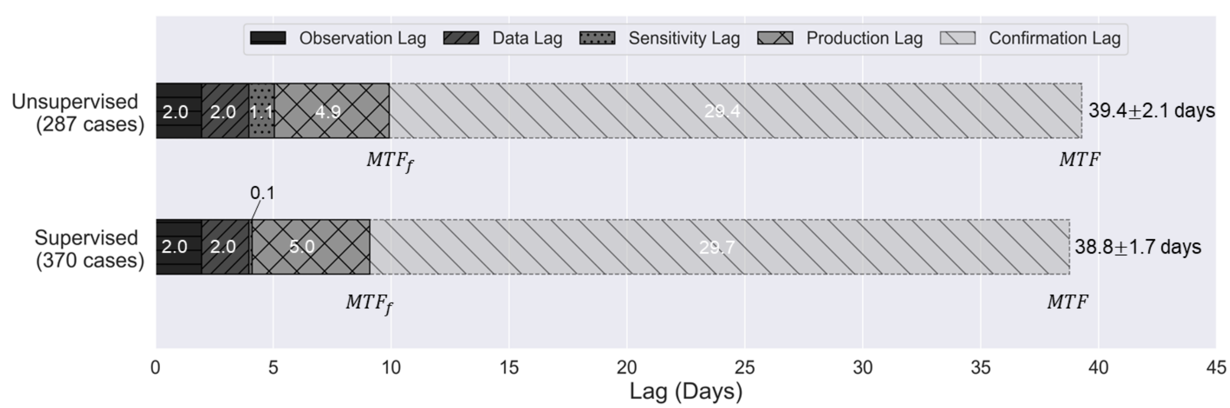

Fig. 8. An assessment of the unsupervised and supervised approach for their different lag components, with their correctly confirmed sample case number shown in the y axis labels. MTL: Mean Time Lag; MTL_f: Mean Time Lag for the First Alert.

4.3 Individual Disturbance Assessments

Fig. 9 shows that individual disturbance types presented different sigmoid curves and lag metrics. For the detection level, "Kentucky flood" (Fig. 9C) received the quickest alerting (the Level-off Point is (9 days, 0.94 F_1 score)) from the NRT platform; "Construction" had the longest latency (the Level-off Point is (43 days, 0.68 F_1 score)) which is possibly due to the fact that the initial stage of a construction project (e.g., land clearing) often yields small-area and unobvious spectral signals; two ephemeral disturbances, "Kentucky Flood" and "Hurricane Ian", presented an inverted U-shaped sigmoid curve while the other three were S-shaped. This indicates that some patches affected by ephemeral disturbances experienced rapid recovery. For the confirmation level, F_1 scores for two ephemeral disturbances dropped dramatically compared to the detection level, while the other three remained similar F_1 scores for their Level-Off Point, which explained the significant overall performance difference between the detection and the confirmation levels in Table 4.

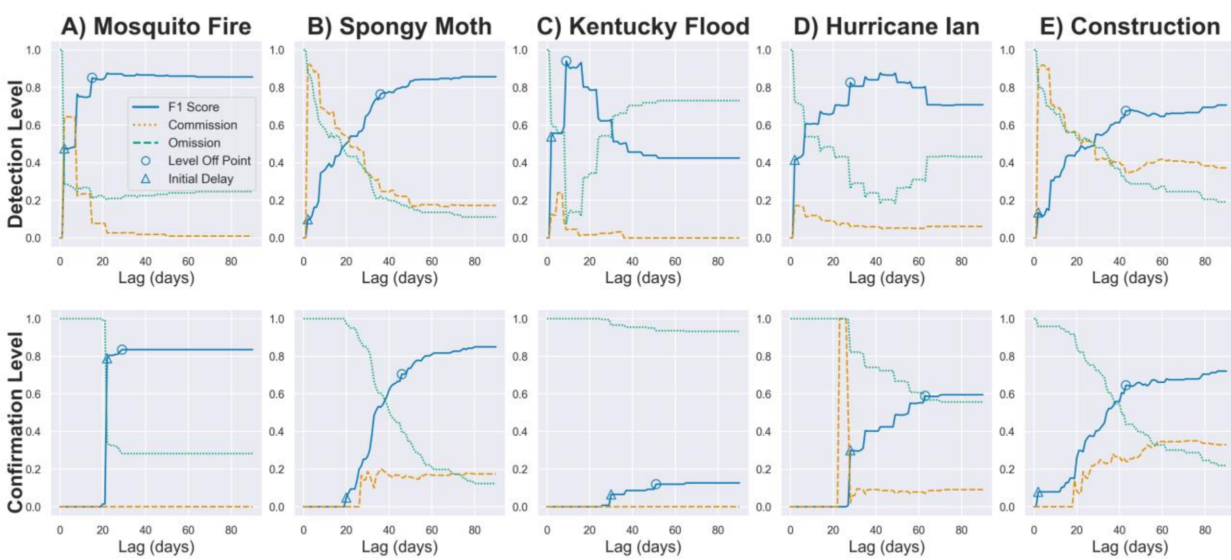

Fig. 9. Sigmoid accuracy curves for individual disturbance events with being marked with the two key latency metrics at the detection and at the confirmation level.

Fig. 10 demonstrates the dynamics of the detection- and the confirmation-level products over time since disturbance. For “Mosquito Fire” (Fig. 10A) and “Spongy Moth” (Fig. 10B), most disturbance regions in the detection level were confirmed (displayed as red polygons) since 5th week in the figure. Differently, the detected patches for two ephemeral disturbances, “Hurricane Ian” (Fig. 10C) and “Kentucky Flood” (Fig. 10D), were not converted into the confirmation-level patches but disappeared after 5th week, as these disturbance events did not last long enough to generate six consistent anomalies. The NRT platform did not successfully map Kentucky Flood at the 1st week for this case, which might be lacking clear observations due to the rainy/cloudy weather accompanying the flooding event (long data lag); once the first post-flood clear observation became available, more flood-related signals were captured mainly on housing damage and soil change, leading to a significant F_1 jump at the 9th day in Fig. 10C (“detection level”).

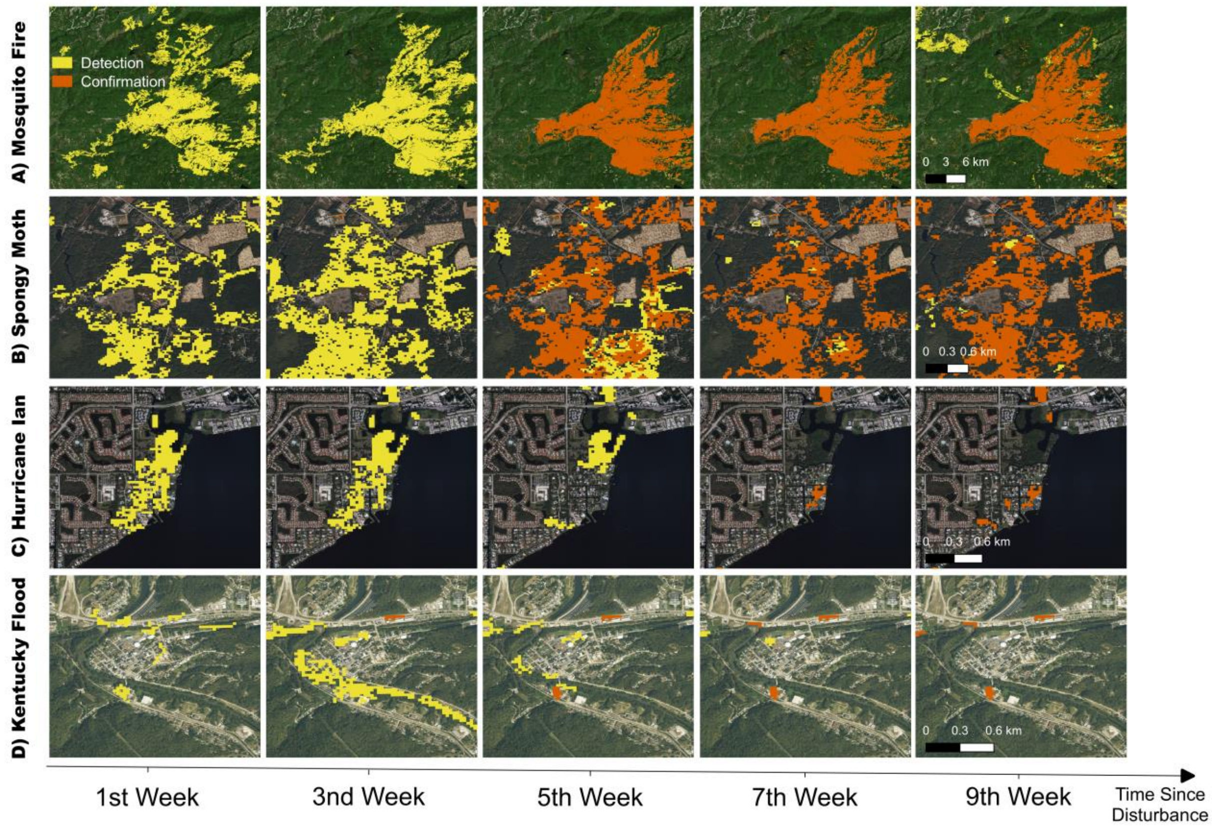

Fig. 10. The dynamics of detection- and confirmation-level products for different disturbance events. The centroid coordinates for the sites are Mosquito Fire (-120.752, 39.056), Spongy Moth (-73.684, 43.144), Hurricane Ian (-81.898, 26.652), and Kentucky Flood (-83.382, 37.553).

5. Discussion

5.1 Comparison to Other NRT Studies

Compared to the study with the closest evaluation method (Bullock et al., 2022), applying CCDC on sentinel-1 time series (i.e., “P2” configuration) reached a Level-off Point (203 days, 0.216 F_1 score) at the confirmation level for detecting deforestation, much worse than the same metric result for the supervised approach for this study (35 days, 0.439 F_1 score). Not mention that we included the ephemeral disturbances which are challenging and significantly impacted our F_1 score at the confirmation level. Reiche et al. (2018) combined observations from six satellites, Sentinel-1, ALOS-2, Landsat 7 and 8, to detect a specific land disturbance, deforestation, and reached MTL as 31 days; Shang et al., (2022) built a method based on HLS datasets with setting four minimum consecutive anomalies for confirmation, reporting a resultant MTL as 35 days. The MTL of the supervised approach seems to be a little longer than the above two studies (38.8 days), but we approached more diversified land disturbances. More important is that we assessed our approach in an operational platform by including observation, data, and production lag assessment, which additionally increases approximately nine extra lag days compared to the previous studies. It is noteworthy that for emergency events, the updating interval of our NRT system could be manually adjusted to a one-day frequency to make the fastest response with zero-day production lag, so that the average lag for alerting the first anomaly for an event (MTL_f) would be further shortened to around half of a week (4.1 days). It would be even faster in the future, with more medium-resolution satellite sensors launched and quicker releasing of reflectance products.

All the previous studies used the unsupervised anomaly approach based on the predefined chi-square threshold, mostly focusing forest disturbances. To our knowledge, this study is the first attempt to build up a sole NRT approach/system intended for various natural disasters and human-induced terrestrial changes. To address the issues of disturbance variety, we designed multifaceted predictors, including the pre-disturbance spectral features that are indicative of background land cover, and post-disturbance spectral features for during-change and post-change signals. With the retrospective analysis on historical disturbances, we were able to generate a more sophisticated decision model for better distinguishing disturbances and commission/non-disturbance errors, especially when the disturbance and commission signals are highly mixed due to insufficient observations in the early window, hence a timelier detection. For future research, the supervised approach is readily expanded to provide NRT mapping for disturbance agents through an incorporation of agent samples.

5.2 Dilemma of Disturbance Confirmation

Almost all previous NRT approaches used consecutive observations for disturbance confirmation. For this study, we used the CCDC default minimum observations ($conse = 6$) for confirming a disturbance patch, which has been well verified in multiple past studies on Landsat-based studies (Brown et al., 2019; Ye et al., 2021a; Zhu et al., 2019). But the $conse$ has not been tested yet on a per-event basis. Especially, it is still challenging for accurately confirming impacted regions of those short-lived events using the current confirmation strategy. The two ephemeral events, “Kentucky Flood” and “Hurricane Ian”, did not lead to permanent land cover conversion, and their spectral signals only lasted for one to three observations. As a result, their omission errors greatly increased after their Level Off Points (Fig. 9C and Fig. 9D). Even with a decreased minimum anomaly number such as $conse = 4$ in (Shang et al., 2022), it is still not likely to accurately detect the events such as flash flooding, which often induces only one anomaly. In contrast, “Spongy Moth” (36 days, 0.76 F_1 score) and “Construction” (43 days, 0.68 F_1 score) had a lag close to the MTL of 38.8 days when they reached their Level Off Points at the detection level, which indicated that confirming a disturbance event with six anomalies ($conse = 6$) was still workable to most non-ephemeral disturbance events. The diversified sigmoid curves and Level Off Points of these disturbance events suggested a future direction for developing agent-based confirmation strategies instead of a universal confirmation rule.

6. Conclusion

We proposed a novel supervised machine learning approach to analyze spectral anomalies from HLS time series. The retrospective analysis mined the early disturbance information from a large pool of spectral anomalies at the stage when only a few observations are available to discriminate disturbance signals. Compared to the unsupervised approach, the latency and accuracy assessment shows the supervised approach brought forward the plateau of sigmoid curve by seven days, with a 0.2 F_1 score improvement. The main advantage of the supervised approach is greatly reducing commission error rate by 27% for the cases of short consecutive anomalies, by applying machine learning on a comprehensive predictor set including spectral change direction, pre-disturbance features, change dates. The lower performance at the confirmation level than at the detection level calls for the new confirmation strategy especially for ephemeral disturbances.

Acknowledgement

This work has been supported by USGS-NASA Landsat Science Team (LST) Program for Toward Near Real-time Monitoring and Characterization of Land Surface Change for the Conterminous US (140G0119C0008). The content of this document does not necessarily represent the views or policies of the Department of the Interior, nor does mention of trade names, commercial products, or organizations imply endorsement by the U.S. Government.

Reference

Andela, N., Morton, D.C., Schroeder, W., Chen, Y., Brando, P.M., Randerson, J.T., 2022. Tracking and classifying Amazon fire events in near real time. Sci. Adv. 8, eabd2713.
Baird, C., 2022. Austin Ranks No. 1 in US for new apartment demand [WWW Document].
Brown, C.F., Brumby, S.P., Guzder-Williams, B., Birch, T., Hyde, S.B., Mazzariello, J., Czerwinski, W., Pasquarella, V.J., Haertel, R., Ilyushchenko, S., 2022. Dynamic World, Near real-time global 10 m land use land cover mapping. Sci. Data 9, 1–17.
Brown, J.F., Tollerud, H.J., Barber, C.P., Zhou, Q., Dwyer, J.L., Vogelmann, J.E., Loveland, T.R., Woodcock, C.E., Stehman, S. V, Zhu, Z., Pengra, B.W., Smith, K., Horton, J.A., Xian, G., Auch, R.F., Sohl, T.L., Sayler, K.L., Gallant, A.L., Zelenak, D., Reker, R.R., Rover, J., 2019. Lessons learned implementing an operational continuous United States national land change monitoring capability: The Land Change Monitoring, Assessment, and Projection (LCMAP)

approach. Remote Sens. Environ. https://doi.org/10.1016/j.rse.2019.111356

Bullock, E.L., Healey, S.P., Yang, Z., Houborg, R., Gorelick, N., Tang, X., Andrianirina, C., 2022. Timeliness in forest change monitoring: A new assessment framework demonstrated using Sentinel-1 and a continuous change detection algorithm. Remote Sens. Environ. 276, 113043.

Centers, N.N., 2023. NOAA National Centers for Environmental Information (NCEI) U.S. Billion-Dollar Weather and Climate Disasters (2023) [WWW Document]. https://doi.org/10.25921/stkw-7w73

Chuvieco, E., Mouillot, F., Van der Werf, G.R., San Miguel, J., Tanase, M., Koutsias, N., García, M., Yebra, M., Padilla, M., Gitas, I., 2019. Historical background and current developments for mapping burned area from satellite Earth observation. Remote Sens. Environ. 225, 45–64.

Claverie, M., Ju, J., Masek, J.G., Dungan, J.L., Vermote, E.F., Roger, J.-C., Skakun, S. V, Justice, C., 2018. The Harmonized Landsat and Sentinel-2 surface reflectance data set. Remote Sens. Environ. 219, 145–161.

Cohen, W.B., Healey, S.P., Yang, Z., Stehman, S. V, Brewer, C.K., Brooks, E.B., Gorelick, N., Huang, C., Hughes, M.J., Kennedy, R.E., 2017. How Similar Are Forest Disturbance Maps Derived from Different Landsat Time Series Algorithms? For. Trees Livelihoods 8, 98.

Diniz, C.G., de Almeida Souza, A.A., Santos, D.C., Dias, M.C., Da Luz, N.C., De Moraes, D.R.V., Maia, J.S., Gomes, A.R., da Silva Narvaes, I., Valeriano, D.M., 2015. DETER-B: The new Amazon near real-time deforestation detection system. IEEE J. Sel. Top. Appl. earth Obs. Remote Sens. 8, 3619–3628.

Doblas, J., Reis, M.S., Belluzzo, A.P., Quadros, C.B., Moraes, D.R. V, Almeida, C.A., Maurano, L.E.P., Carvalho, A.F.A., Sant'Anna, S.J.S., Shimabukuro, Y.E., 2022. DETER-R: An operational near-real time tropical forest disturbance warning system based on Sentinel-1 time series analysis. Remote Sens. 14, 3658.

Eckerstorfer, M., Vickers, H., Malnes, E., Grahn, J., 2019. Near-real time automatic snow avalanche activity monitoring system using Sentinel-1 SAR data in norway. Remote Sens. 11, 2863.

Field, C.B., Barros, V., Stocker, T.F., Dahe, Q., 2012. Managing the risks of extreme events and disasters to advance climate change adaptation: special report of the intergovernmental panel on climate change. Cambridge University Press.

Francini, S., McRoberts, R.E., Giannetti, F., Mencucci, M., Marchetti, M., Scarascia Mugnozza, G., Chirici, G., 2020. Near-real time forest change detection using PlanetScope imagery. Eur. J. Remote Sens. 53, 233–244.

Giglio, L., Loboda, T., Roy, D.P., Quayle, B., Justice, C.O., 2009. An active-fire based burned area mapping algorithm for the MODIS sensor. Remote Sens. Environ. 113, 408–420.

Gill, S.K., Kaplan, A.S., 2021. A retrospective chart review study of symptom onset, diagnosis, comorbidities, and treatment in patients with binge eating disorder in Canadian clinical practice. Eat. Weight Disord. Anorexia, Bulim. Obes. 26, 1233–1242.

Hansen, M.C., Krylov, A., Tyukavina, A., Potapov, P. V, Turubanova, S., Zutta, B., Ifo, S., Margono, B., Stolle, F., Moore, R., 2016. Humid tropical forest disturbance alerts using Landsat data. Environ. Res. Lett. 11, 34008.

Hawbaker, T.J., Vanderhoof, M.K., Schmidt, G.L., Beal, Y.-J., Picotte, J.J., Takacs, J.D., Falgout,

J.T., Dwyer, J.L., 2020. The Landsat Burned Area algorithm and products for the conterminous United States. Remote Sens. Environ. 244, 111801.
Hess, D.R., 2004. Retrospective studies and chart reviews. Respir. Care 49, 1171–1174.
Johnson, E.W., Wittwer, D., 2008. Aerial detection surveys in the United States. Aust. For. 71, 212–215.
Kaji, A.H., Schriger, D., Green, S., 2014. Looking through the retrospectoscope: reducing bias in emergency medicine chart review studies. Ann. Emerg. Med. 64, 292–298.
Karimiziarani, M., Moradkhani, H., 2023. Social response and Disaster management: Insights from twitter data Assimilation on Hurricane Ian. Int. J. Disaster Risk Reduct. 95, 103865.
Latifovic, R., Homer, C., Ressl, R., Pouliot, D., Hossain, S.N., Colditz, R.R., Olthof, I., Giri, C.P., Victoria, A., 2016. 20 North American Land-Change Monitoring System. Remote Sens. L. use L. Cover 303.
Liang, L., Chen, Y., Hawbaker, T.J., Zhu, Z., Gong, P., 2014. Mapping mountain pine beetle mortality through growth trend analysis of time-series landsat data. Remote Sens. https://doi.org/10.3390/rs6065696
Martínez-Ramos, M., Ortiz-Rodríguez, I.A., Piñero, D., Dirzo, R., Sarukhán, J., 2016. Anthropogenic disturbances jeopardize biodiversity conservation within tropical rainforest reserves. Proc. Natl. Acad. Sci. U. S. A. https://doi.org/10.1073/pnas.1602893113
Martinis, S., Plank, S., Ćwik, K., 2018. The use of Sentinel-1 time-series data to improve flood monitoring in arid areas. Remote Sens. 10, 583.
Olsson, P.-O., Lindström, J., Eklundh, L., 2016. Near real-time monitoring of insect induced defoliation in subalpine birch forests with MODIS derived NDVI. Remote Sens. Environ. 181, 42–53. https://doi.org/10.1016/j.rse.2016.03.040
Pasquarella, V., Bradley, B., Woodcock, C., 2017. Near-Real-Time Monitoring of Insect Defoliation Using Landsat Time Series. Forests. https://doi.org/10.3390/f8080275
Peters, E.B., Wythers, K.R., Bradford, J.B., Reich, P.B., 2013. Influence of disturbance on temperate forest productivity. Ecosystems 16, 95–110.
Reiche, J., Hamunyela, E., Verbesselt, J., Hoekman, D., Herold, M., 2018. Improving near-real time deforestation monitoring in tropical dry forests by combining dense Sentinel-1 time series with Landsat and ALOS-2 PALSAR-2. Remote Sens. Environ. 204, 147–161.
Reiche, J., Mullissa, A., Slagter, B., Gou, Y., Tsendbazar, N.-E., Odongo-Braun, C., Vollrath, A., Weisse, M.J., Stolle, F., Pickens, A., 2021. Forest disturbance alerts for the Congo Basin using Sentinel-1. Environ. Res. Lett. 16, 24005.
Reymondin, L., Jarvis, A., Perez-Uribe, A., Touval, J., Argote, K., Rebetez, J., Guevara, E., Mulligan, M., 2012. Terra-i: A methodology for near real-time monitoring of habitat change at continental scales using modis-ndvi and trmm. CIAT-Terra-i.
Rollins, M.G., 2009. LANDFIRE: a nationally consistent vegetation, wildland fire, and fuel assessment. Int. J. Wildl. Fire 18, 235–249.
Ryan, K.C., Opperman, T.S., 2013. LANDFIRE–A national vegetation/fuels data base for use in fuels treatment, restoration, and suppression planning. For. Ecol. Manage. 294, 208–216.
Seidl, R., Schelhaas, M.-J., Rammer, W., Verkerk, P.J., 2014. Increasing forest disturbances in Europe and their impact on carbon storage. Nat. Clim. Chang. 4, 806–810.
Shang, R., Zhu, Z., Zhang, J., Qiu, S., Yang, Z., Li, T., Yang, X., 2022. Near-real-time monitoring of land disturbance with harmonized Landsats 7–8 and Sentinel-2 data. Remote Sens.

Environ. 278, 113073.

Shimabukuro, Y., Duarte, V., Anderson, L., Valeriano, D., Arai, E., Freitas, R., Rudorff, B.F., Moreira, M., 2006. Near real time detection of deforestation in the Brazilian Amazon using MODIS imagery. Ambient. e Agua-An Interdiscip. J. Appl. Sci. 1, 37–47.

Tang, X., Bullock, E.L., Olofsson, P., Estel, S., Woodcock, C.E., 2019. Near real-time monitoring of tropical forest disturbance: New algorithms and assessment framework. Remote Sens. Environ. 224, 202–218.

Teater, D., 2023. Aquatics Specialist Report Mosquito Fire Burned Area Emergency Response (BAER) Assessment Tahoe National Forest.

Vargas, C., Montalban, J., Leon, A.A., 2019. Early warning tropical forest loss alerts in Peru using Landsat. Environ. Res. Commun. 1, 121002.

Vassar, M., Matthew, H., 2013. The retrospective chart review: important methodological considerations. J. Educ. Eval. Health Prof. 10.

Verbesselt, J., Zeileis, A., Herold, M., 2012. Near real-time disturbance detection using satellite image time series. Remote Sens. Environ. 123, 98–108.

Woodcock, C.E., Allen, R., Anderson, M., Belward, A., Bindschadler, R., Cohen, W., Gao, F., Goward, S.N., Helder, D., Helmer, E., Nemani, R., Oreopoulos, L., Schott, J., Thenkabail, P.S., Vermote, E.F., Vogelmann, J., Wulder, M.A., Wynne, R., 2008. Free access to Landsat imagery. Science (80-.). 320, 1011–1011. https://doi.org/10.1126/science.320.5879.1011a

Wulder, M.A., Coops, N.C., Roy, D.P., White, J.C., Hermosilla, T., 2018. Land cover 2.0. Int. J. Remote Sens. 39, 4254–4284.

Xian, G.Z., Smith, K., Wellington, D., Horton, J., Zhou, Q., Li, C., Auch, R., Brown, J.F., Zhu, Z., Reker, R.R., 2022. Implementation of the CCDC algorithm to produce the LCMAP Collection 1.0 annual land surface change product. Earth Syst. Sci. Data 14, 143–162.

Yang, X., Zhu, Zhe, Qiu, S., Kroeger, K.D., Zhu, Zhiliang, Covington, S., 2022. Detection and characterization of coastal tidal wetland change in the northeastern US using Landsat time series. Remote Sens. Environ. 276, 113047.

Ye, S., Rogan, J., Zhu, Z., Eastman, J.R., 2021a. A near-real-time approach for monitoring forest disturbance using Landsat time series: stochastic continuous change detection. Remote Sens. Environ. https://doi.org/10.1016/j.rse.2020.112167

Ye, S., Rogan, J., Zhu, Z., Hawbaker, T.J., Hart, S.J., Andrus, R.A., Meddens, A.J.H., Hicke, J.A., Eastman, J.R., Kulakowski, D., 2021b. Detecting subtle change from dense Landsat time series: Case studies of mountain pine beetle and spruce beetle disturbance. Remote Sens. Environ. https://doi.org/10.1016/j.rse.2021.112560

Ye, S., Zhu, Z., Cao, G., 2023. Object-based continuous monitoring of land disturbances from dense Landsat time series. Remote Sens. Environ. 287, 113462.

Yu, L., Du, Z., Dong, R., Zheng, J., Tu, Y., Chen, X., Hao, P., Zhong, B., Peng, D., Zhao, J., 2022. FROM-GLC Plus: toward near real-time and multi-resolution land cover mapping. GIScience Remote Sens. 59, 1026–1047.

Zhu, Z., Gallant, A.L., Woodcock, C.E., Pengra, B., Olofsson, P., Loveland, T.R., Jin, S., Dahal, D., Yang, L., Auch, R.F., 2016. Optimizing selection of training and auxiliary data for operational land cover classification for the LCMAP initiative. ISPRS J. Photogramm. Remote Sens. 122, 206–221.

Zhu, Z., Woodcock, C.E., 2014. Continuous change detection and classification of land cover

using all available Landsat data. Remote Sens. Environ. 144, 152–171.
Zhu, Z., Zhang, J., Yang, Z., Aljaddani, A.H., Cohen, W.B., Qiu, S., Zhou, C., 2020. Continuous monitoring of land disturbance based on Landsat time series. Remote Sens. Environ. 238, 111116.
Zhu, Z., Zhang, J., Yang, Z., Aljaddani, A.H., Cohen, W.B., Qiu, S., Zhou, C., 2019. Continuous monitoring of land disturbance based on Landsat time series. Remote Sens. Environ. https://doi.org/10.1016/j.rse.2019.03.009